

Miscellaneous Lasing Actions in Organo-Lead Halide Perovskite Films

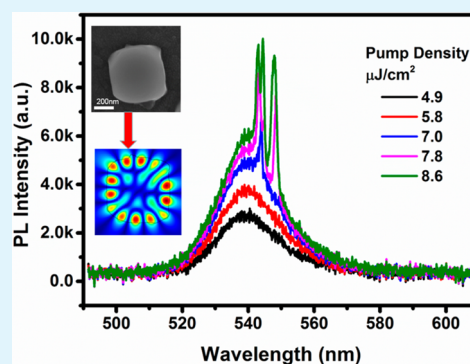
Zonghui Duan, Shuai Wang,¹ Ningbo Yi, Zhiyuan Gu, Yisheng Gao, Qinghai Song,^{2*} and Shumin Xiao^{1*}

State Key Laboratory on Tunable Laser Technology, Ministry of Industry and Information Technology Key Lab of Micro-Nano Optoelectronic Information System, Shenzhen Graduate School, Harbin Institute of Technology, Shenzhen 518055, China

Supporting Information

ABSTRACT: Lasing actions in organo-lead halide perovskite films have been heavily studied in the past few years. However, due to the disordered nature of synthesized perovskite films, the lasing actions are usually understood as random lasers that are formed by multiple scattering. Herein, we demonstrate the miscellaneous lasing actions in organo-lead halide perovskite films. In addition to the random lasers, we show that a single or a few perovskite microparticles can generate laser emissions with their internal resonances instead of multiple scattering among them. We experimentally observed and numerically confirmed whispering gallery (WG)-like microlasers in polygon shaped and other deformed microparticles. Meanwhile, owing to the nature of total internal reflection and the novel shape of the nanoparticle, the size of the perovskite WG laser can be significantly decreased to a few hundred nanometers. Thus, wavelength-scale lead halide perovskite lasers were realized for the first time. All of these laser behaviors are complementary to typical random lasers in perovskite film and will help the understanding of lasing actions in complex lead halide perovskite systems.

KEYWORDS: lead halide perovskite, lasing actions, wavelength-scale, whispering gallery mode, Q-factor



INTRODUCTION

Organo-lead halide perovskites have been intensively studied due to their great potentials in solar cells.^{1,2} In the past six years, the power conversion efficiency (PCE) of lead halide perovskites has been dramatically increased from a few percent to more than 22.1%, which is even higher than the record PCE value of CdTe thin film solar cells. The rapid progress in solar cells has also triggered advances of other perovskite-based optoelectronic devices such as light emitting devices and photodetectors.^{3–6} In 2014, Xing et al.⁷ and Deschler et al.⁸ independently revealed the optical amplification in lead halide perovskites. The optical gain of lead halide perovskites has been reported as high as $3200 \pm 830 \text{ cm}^{-1}$, which is comparable to the gain coefficient of single crystalline GaAs.⁹ Associated with the fact that lead halide perovskite can be directly synthesized from solution, this material suddenly becomes very promising for laser applications.¹⁰ More than the cost-effective nature, the recently developed fabrication techniques can simply fabricate high quality microdisk lasers with arbitrary shapes and high repeatability, which are actually difficult to be realized with III-nitride semiconductors. Most importantly, the bandgap and emission wavelengths of lead halide perovskites can be widely tuned from ultraviolet to near-infrared either by controlling the stoichiometry in solution or by postsynthetic ion-exchange.^{11–14} Thus, lead halide perovskites can effectively surpass the “green gap” between III-nitrides and III-phosphides.

In the past two years, many types of lead halide perovskite lasers have been experimentally demonstrated, and a number of practical applications have been proposed. Soon after the discovery of optical gain in lead halide perovskite film, whispering gallery (WG)-based lead halide perovskite lasers have been successfully realized in a number of polygon-shaped microplates, e.g. hexagon, square, triangle, etc.^{15–17} By synthesizing single crystalline nanorods, Zhu et al. reported the lead halide perovskite nanowire lasers with record low threshold (220 nJ/cm^2) and record high Q factor (3600).^{15,18,19} In 2016, single-mode WG lasers and high-density uniform laser array were achieved from the transverse planes of lead halide perovskites microrods by tailoring the substrate.^{20,21} Meanwhile, the laser emissions from lead halide perovskites were successfully coupled to waveguide or tapered fiber, making perovskite microlaser suitable for integration with conventional photonic systems.^{22,23} Very recently, distributed feedback Bragg lasers,^{24–26} photonic crystal lasers,²⁷ and WG lasers have also been achieved by combining the lead halide perovskite films with different nanostructures such as gratings, two-dimensional photonic crystals, and microspheres.

In addition to all of these well-designed microlasers, the lasing actions that are directly formed within the perovskite

Received: January 27, 2017

Accepted: June 2, 2017

Published: June 2, 2017

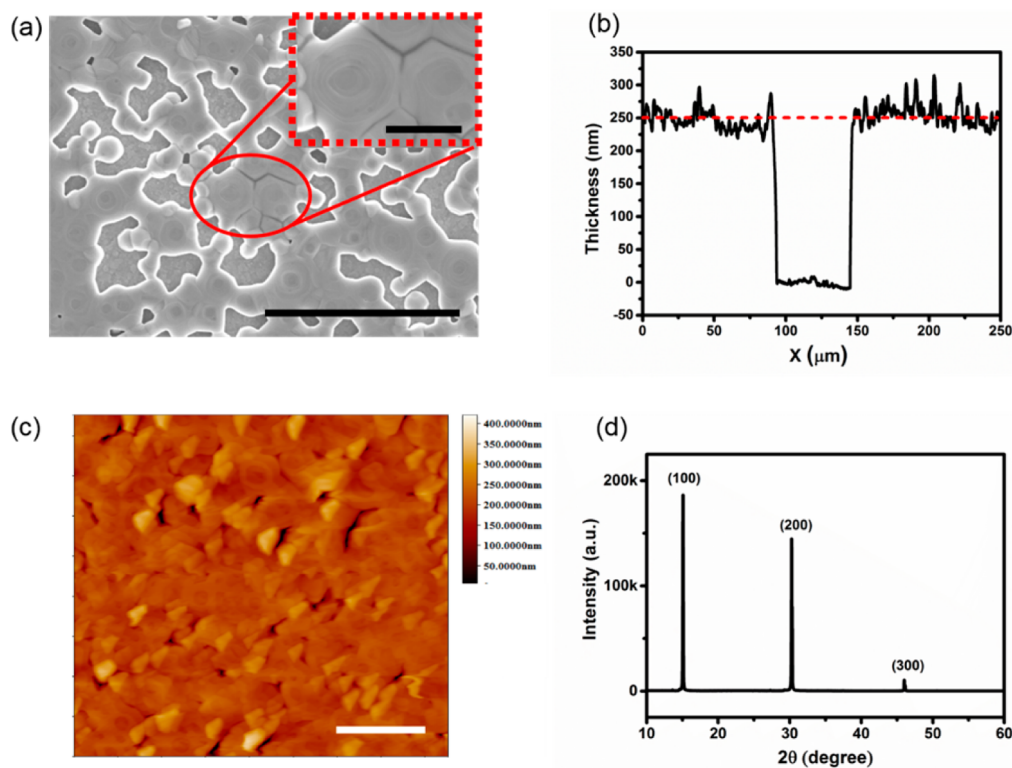


Figure 1. (a) Representative SEM image of $\text{CH}_3\text{NH}_3\text{PbBr}_3$ films; the scale bar is $5\ \mu\text{m}$. The inset is the amplified image of the marked area, wherein the scale bar is $1\ \mu\text{m}$. (b and c) Thickness analyses and AFM image of $\text{CH}_3\text{NH}_3\text{PbBr}_3$ films, respectively. The red dotted line shown in panel b indicates the average thickness of the MAPbBr_3 film is around $250\ \text{nm}$. (d) XRD spectrum of $\text{CH}_3\text{NH}_3\text{PbBr}_3$ films. The scale bar in panel c is $4\ \mu\text{m}$.

films have also been widely studied.^{28–30} Typically, because no cavity boundaries have been designed within these films, the laser emissions are considered as random lasers that take the advantage of disorder in perovskite films.^{31–33} This intuitive understanding is right but not very accurate in some cases. In a number of lead halide perovskite films, the sizes of domains or units are comparable to or even larger than the lasing wavelength.^{27,34–36} In this sense, these types of scatters can not only scatter the light but also confine the light within them with either reflection or total internal reflection.^{37,38} Therefore, while aperiodic or random laser peaks have been experimentally observed, they might not be formed by the multiple scattering among the disorder domains or subunits. Instead, they are also possibly formed within these scatters that have random sizes. Herein, we selectively pumped the lead halide perovskite films and study the miscellaneous lasing actions within them.

RESULTS AND DISCUSSIONS

Preparation of Lead Halide Perovskite Film. The lead halide perovskite film was synthesized with a very simple spin-coating method. Basically, the $\text{CH}_3\text{NH}_3\text{PbBr}_3$ precursor was prepared by dissolving PbBr_2 and $\text{CH}_3\text{NH}_3\text{Br}$ with a 1:1 molar ratio in dimethyl sulfoxide to give a concentration of 40 wt %, followed by a 4 h of stirring at $60\ ^\circ\text{C}$. Then, $50\ \mu\text{L}$ of $\text{CH}_3\text{NH}_3\text{PbBr}_3$ precursor was dropped on the ITO glass substrates and spun at 5000 rpm for 1 min. During the whole spin-coating process, the perovskite films were blown by dry nitrogen gas with a pressure $0.03\ \text{MPa}$ through a funnel. At the 37th second of spinning, $60\ \mu\text{L}$ of chlorobenzene was quickly dropped on the film, and the transparent colorless film turned into yellow immediately. Notably, the hydrophilicity also played an important role in the formation of uniform and dense lead

halide perovskite film. In the current experiment, the ITO substrates were cleaned by sonication in acetone, isopropanol, and deionized water for 15 min, respectively. Subsequently, they were treated with oxygen plasma (MYCRO, FEMTO6SA) for 5 min to achieve the hydrophilic surface.

Figure 1a shows the top-view scanning electron microscope (SEM) image of the synthesized $\text{CH}_3\text{NH}_3\text{PbBr}_3$ films. While the particles are closely packaged and the film is almost homogeneous in a wide range, there are still some pinholes (Figure S1). The sizes of particles are approximately a few hundred nanometers. Nevertheless, they increase dramatically to several micrometers around the defect regions and pinholes. Figure 1b shows that the thickness of the film is around $250\ \text{nm}$. Meanwhile, the surface morphology of the perovskite film has also been studied with atomic force microscopy (AFM). The results are shown in Figure 1c. The average roughness analyzed by C-SPM Image software within a $17 \times 17\ \mu\text{m}$ area is $31.6\ \text{nm}$, which is close to conventional perovskite films. In addition to study of the morphological information, the $\text{CH}_3\text{NH}_3\text{PbBr}_3$ perovskite film was also studied by X-ray diffraction (XRD) to understand the corresponding crystal structures. As shown in Figure 1d, three dominant peaks can be seen at $2\theta = 15.08^\circ$, 30.25° , and 46.01° , respectively. The other peaks are more than 2 orders of magnitude smaller. These three peaks can be indexed to (100), (200), and (300) planes of the cubic phase lead halide perovskite crystals and match the reports of single crystalline perovskite microplates and microrods well.²² In addition, the $\text{CH}_3\text{NH}_3\text{PbBr}_3$ particles were also measured with transmission electron microscopy (TEM) (see Figure S1 in the Supporting Information), and it is easy to confirm that high quality crystals were formed within

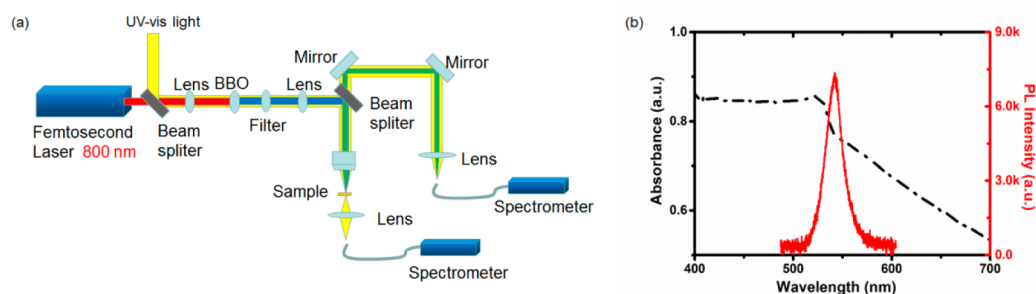


Figure 2. (a) The schematic picture of homemade setup for PL and lasing measurement. (b) The absorbance and photoluminescence spectrum of $\text{CH}_3\text{NH}_3\text{PbBr}_3$ films.

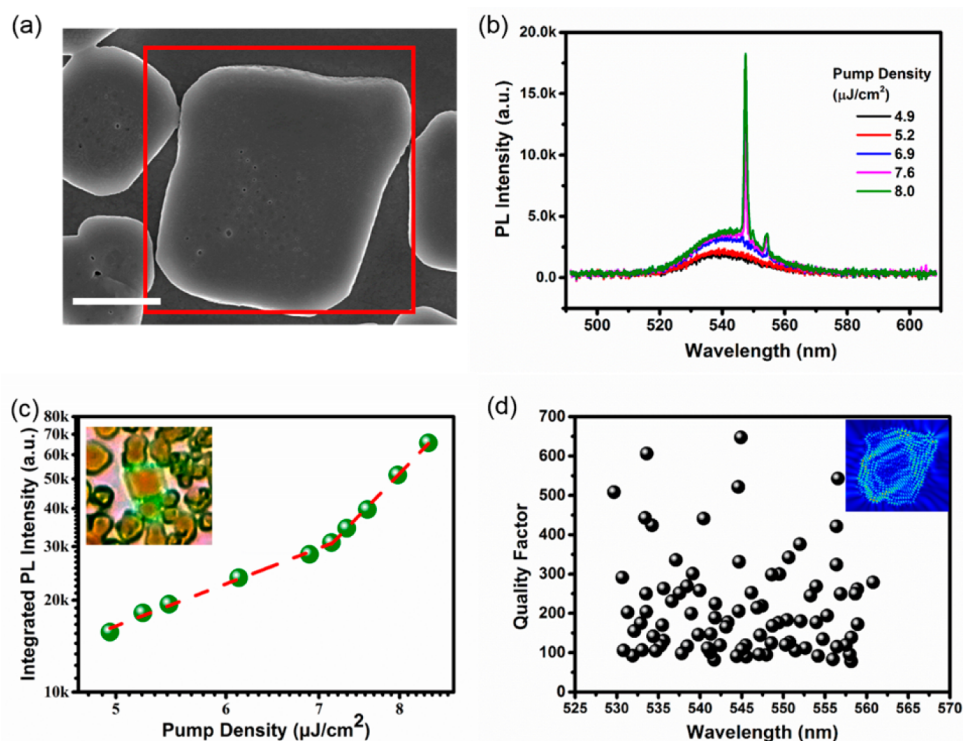


Figure 3. (a) A SEM image of $\text{CH}_3\text{NH}_3\text{PbBr}_3$ particles. The scale bar is $2 \mu\text{m}$. (b) The PL spectrum of the $\text{CH}_3\text{NH}_3\text{PbBr}_3$ particle, which was marked with a red rectangle in panel a. (c) Integrated PL intensity as a function of excitation density. The inset is the fluorescence microscopy image of $\text{CH}_3\text{NH}_3\text{PbBr}_3$ particles. (d) Calculated Q factor as a function of wavelength, where the refractive index n_{eff} of $\text{CH}_3\text{NH}_3\text{PbBr}_3$ is set at 2.55, and the material dispersion has been neglected. The inset of panel d is the electromagnetic field distribution of the perovskite particle.

the perovskite film even though they do not have very standard structural shapes such as squares or hexagons.

Optical Characterization. The synthesized $\text{CH}_3\text{NH}_3\text{PbBr}_3$ films were measured with a home-built transmission/reflection microscopy setup (Figure 2a). A white light from a lamp was focused using a $40\times$ objective lens onto the top-surface of the samples. Typically, the microsized samples can be clearly seen under microscope. In the case of small samples ($\sim 1 \mu\text{m}$), their locations are determined with the relative distances from samples to relatively large particles around them. The transmission (T) and reflection (R) spectra were measured by a CCD coupled spectrometer (Acton SpectroPro 2700), and the light extinction spectrum (Ext) was calculated with $\text{Ext} = 100 - T - R$. The obtained absorption spectrum is plotted as the dashed line in Figure 2b. We can observe that the extinction of $\text{CH}_3\text{NH}_3\text{PbBr}_3$ thin film has a clear step-like increase at $\sim 540 \text{ nm}$, which has been identified as the principle interband transition inside the perovskite thin film. However, there are

two obvious differences between Figure 2b and the absorption of the single crystalline microplate. In the latter case, the band edge corresponds to a wavelength around 550 nm . Meanwhile, the absorption at a longer wavelength range is negligibly small and almost flat. Here, the light extinction increases slightly and decreases with the increase in wavelength. An extra extinction peak was formed at around 556 nm , which is simply caused by the light scattering inside the perovskite film. As shown in the SEM and AFM images, the perovskite film is formed by numerous nanoparticles that can strongly scatter light and generate additional light extinction at longer wavelengths.

The photoluminescence (PL) of $\text{CH}_3\text{NH}_3\text{PbBr}_3$ thin film was also recorded by replacing the white light source with a frequency doubled Ti:sapphire laser (400 nm , 100 fs pulse duration, 1 K Hz repetition rate). Similarly, a $40\times$ objective lens was used to focus the pumping laser into a spot with diameter around $20 \mu\text{m}$. As the solid line shown in Figure 2b, a broad PL peak can be observed at 540 nm . The corresponding full width

half-maximum (fwhm) is around 25 nm. Both the central wavelength and fwhm of the PL are consistent with the single crystalline $\text{CH}_3\text{NH}_3\text{PbBr}_3$ microplates or microrods. In many perovskite films, the fwhm values of PL are much larger than the value of single crystal microplate due to the imperfect or incomplete transition from PbBr_2 to $\text{CH}_3\text{NH}_3\text{PbBr}_3$ perovskite.^{20,39} Here, the consistency between our experimental results and the PL of single crystal clearly confirms again the high quality of crystallization during the synthesis process.

WG Lasers in Chaotic Microparticles. From the SEM image, XRD measurement, and PL spectrum, we know that high quality $\text{CH}_3\text{NH}_3\text{PbBr}_3$ crystals were synthesized inside the thin films. Therefore, it is natural to consider the possible laser emissions from the lead halide perovskite films. The optical pumping setup is still the same as that in Figure 2a except that the pumping density of Ti:sapphire laser was increased. Meanwhile, the detecting position was changed for different experiments. Initially, the sample was pumped through the objective lens in Figure 2a and collected from the side of the substrate. Similar to previous reports,^{28,29} clear light amplification and several discrete narrow peaks have been observed. As mentioned above, the disordered thin films are very complicated. The observed narrow peaks can be attributed to either the multiple scattering of the particles or the internal resonances within individual particles. Thus, the lasing actions in perovskite films must be treated with caution.

To identify the efforts of resonances in individual particles, we shifted the detecting position back to the normal direction with the objective lens and decreased the pumping area to around 20 μm in diameter, which can cover only a few particles simultaneously. Figure 3 summarizes one of the experimental results (see the other experimental results in the Supporting Information). The top-view SEM image (Figure 3a) shows that the particle is essentially similar to a rectangle with rounded corners even though the sidewalls are not as flat as single crystals. The side lengths of the particles are around 4.86 and 6.11 μm , respectively, and the thickness of the whole perovskite film is around 250 nm. Considering the situation that the particle is mostly isolated from the nearby objects and the size of particle is much larger than the emission wavelength, a series of relatively high Q resonances and lasing modes can be formed by total internal reflection within the particle.

Figure 3b shows the emission spectra at different pumping densities. As the pumping density is low, the emission spectrum shows a broad PL peak, and the intensity grows slowly with the increase in pumping density. Once the pumping density is above 7.2 $\mu\text{J}/\text{cm}^2$, two sharp peaks emerge at 546.4 and 554.7 nm, respectively. The intensities of the two peaks increase dramatically when the pumping density is further increased, and a superliner power slope is generated, as shown in Figure 3c. Associated with the appearance of sharp laser peaks, the fwhm of emission spectrum drastically decreases from ~ 25 to below 1 nm, and a bright spot appears in the fluorescent microscope image (see the inset in Figure 3c). On the basis of previous reports, the lasing actions in square-like microparticle can thus be confirmed.

Interestingly, here, the lasing actions are found to be independent of the pumping position and pumping size. This is intrinsically different from the typical random lasers. Meanwhile, bright spots can be observed only at the edges of one microparticle. The regions nearby the microparticle usually support broad photoluminescence instead of laser emissions (detailed experimental results can be seen in Figures S6–S9 in

the Supporting Information). In this sense, the observed laser emissions can no longer be explained by multiple scattering. To fully understand the observed lasers, we numerically calculated the resonant modes within the particle with a finite element method (Comsol Multiphysics 4.3a). The cavity boundary is directly obtained from the top-view SEM image. Because the in-plane dimensions are much larger than the thickness, the microparticle was simplified into a two-dimensional object by using the effective refractive index n_{eff} . The calculated results are summarized in Figure 3d. Here, the refractive index n_{eff} is set at 2.55, and the material dispersion was neglected. Around the lasing wavelength range, a series of relatively high Q modes ($Q \sim 500\text{--}700$) can be observed. Different from the conventional square microcavity, these modes are randomly distributed in the spectrum, and the mode spacing varies between 4 to 10 nm. The inset in Figure 3d shows the field pattern of resonant mode at 547.6 nm. Although the high Q mode depicts a diamond-like shape, the orbit is not closed as the conventional WG mode (Figure S2 in the Supporting Information), and the electromagnetic field is randomly distributed to almost the whole space.

The above differences are caused by the irregular cavity shape. While the particle is close to a square (Figure 3a), the corners of the cavities are partially rounded, and the sidewalls are very rough and concave. On the basis of the previous report, the rough surface itself can generate strong scattering and introduce chaotic behaviors to the optical microcavity.⁴⁰ In addition, the concave surfaces will also diffuse the light into different directions and smear out the stable orbits. In this sense, the experimentally obtained irregular cavity shape is almost fully chaotic in phase space. In chaotic microcavities, the electromagnetic waves are no longer confined by total internal reflection along the well-designed diamond mode. Instead, they are confined by the dynamical localization. Therefore, the corresponding Q factors are significantly spoiled, and the field patterns are also randomly distributed (see the field pattern of another high Q mode in Figure S2).

The lasing actions are not restricted in particular microparticles. In principle, due to the fast crystallizing process, most of particles in lead halide films, especially the large particles, are similar but quite different from the square or rectangle shapes of typical single crystalline microstructure. We observed lasing actions from many microparticles (see another example in the Supporting Information). Actually, there are also some microparticles that are strongly deformed from square shape but can still support the lasing actions independently (see Figures S4 and S5 in the Supporting Information). Moreover, the lasing actions are not only limited in an isolated microparticle. In some cases, they can also be generated with several connected nanoparticles (see Figure S3 in the Supporting Information).

Wavelength-Scale Microlasers. Because the lead halide perovskite lasers have potential applications in the integrated photonic network, it is natural to consider the possibility of realizing all three-dimensional wavelength scale perovskite devices. For conventional semiconductor microdisks, wavelength scale and subwavelength scale microdisks have already been successfully demonstrated.⁴¹ In case of lead halide perovskite lasers, most of them are as large as micrometer or tens of micrometers in at least one-dimension. Up to now, submicrometer and wavelength-scale perovskite microlasers are still absent even though the subwavelength scale microwires have been experimentally obtained for a long time. This is

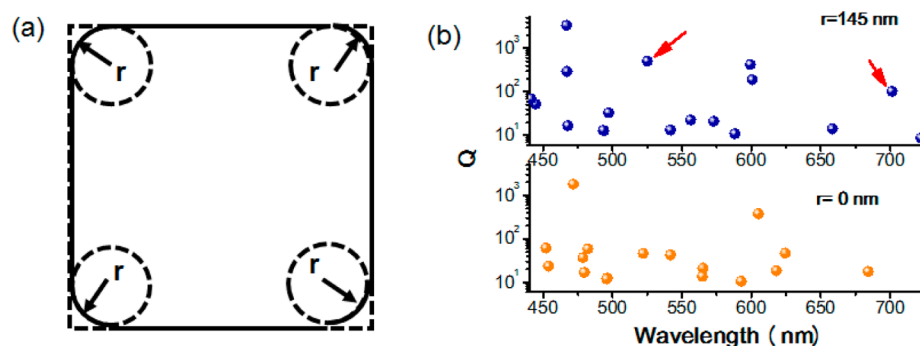


Figure 4. (a) Representative image of square cavity of $\text{CH}_3\text{NH}_3\text{PbBr}_3$ with rounded corners. (b) The simulated quality factor as a function of wavelength with two different rounded radii of the square cavity.

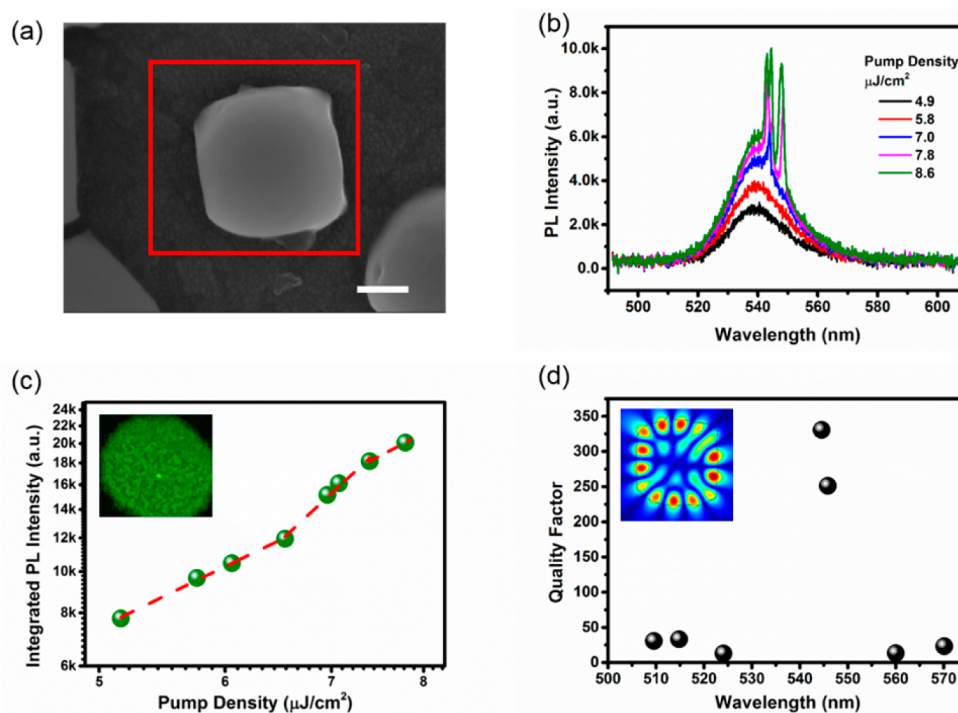


Figure 5. (a) SEM image of $\text{CH}_3\text{NH}_3\text{PbBr}_3$ particles. The scale bar is 200 nm. (b) PL spectra of $\text{CH}_3\text{NH}_3\text{PbBr}_3$ particle, which is marked with red rectangle in panel a. (c) Integrated PL spectrum of the $\text{CH}_3\text{NH}_3\text{PbBr}_3$ particle. The inset in panel c is the fluorescent microscopy image of $\text{CH}_3\text{NH}_3\text{PbBr}_3$ particles. (d) The calculated Q factor as a function of wavelength. The inset of panel d is the electromagnetic field of the higher Q mode distributed in the perovskite particle.

mainly caused by the properties of light confinement in polygon shaped cavities. In principle, the Q factors of resonances are exponentially dependent on the cavity size. When the cavity size is reduced to wavelength or subwavelength scale, the Q factors are usually very low, especially for the polygon shaped microcavities. Taking $\text{CH}_3\text{NH}_3\text{PbBr}_3$ as an example, both the single crystal microplate and the transverse plane of the microrod are rectangle or square shapes. In such cavities, high Q resonances are confined by the total internal reflection along the diamond shaped orbit. With the reduction of cavity size, the diamond orbits are significantly influenced by two efforts. First, the Q factors are significantly spoiled as the field distributions around the corners are increased (relating to the boundary-wave leakage and pseudointegrable leakage). Last but not least, the optical length of the diamond orbit is very short, and the mode spacing between two high Q resonances is intensively large in small cavities (see an example in Figure 4b). Considering the

narrow spectral range of perovskite emission (~ 25 to 30 nm), the latter one makes it extremely difficult to form a three-dimensional perovskite lasers.

Interestingly, this obstacle can be tackled in the lead halide perovskite films. As shown in Figures 3 and 4, while the particle boundaries are close to polygons, most of them have rounded corners and convex boundaries, making it possible for the high Q resonances to be confined along the cavity boundary instead of the diamond orbits (Figure 4). In this sense, both of cavity Q factors and mode spacings can be improved. One example is shown in Figure 4. As depicted in Figure 4a, the resonator is a square cavity with rounded corners. With the increase in radius r , the Q factors of initial diamond resonances are increased. Most importantly, the additional high Q modes appear between original high Q resonances, making the mode spacing halved. Further increasing the rounding radius r , high order WG-like resonances can also be excited. Therefore, there are more

chances to form wavelength scale lasers in lead halide perovskite films.

In our experiment, we indeed observed lasing actions from this type of tiny particle. One example is shown in Figure 5. From the top-view SEM image in Figure 5a, we can see that the boundary of microparticle still follows a square-like shape.⁴² The side length of particle is around 590 nm, which is very close to the emission wavelength of $\text{CH}_3\text{NH}_3\text{PbBr}_3$. Similar to the above devices, here, the tiny particle is also disconnected to the nearby particles. The smallest separation distance is 200 nm, which is about half the wavelength. Consequently, the coupling between nearby particles is negligibly small, and the tiny particle can resonant and lase independently.⁴³

When the pumping density is low, broad PL centered at 540 nm is observed. The fwhm is still around 25 nm. Both the central wavelength and fwhm are close to conventional $\text{CH}_3\text{NH}_3\text{PbBr}_3$ single crystal. On increasing the pumping density from 5 to $6.9 \mu\text{J}/\text{cm}^2$, a sharp peak appears around 545.2 nm. Further increasing the pumping density, another sharp peak emerges at around 548.6 nm. The fwhm values of these peaks are around 0.7 nm, which are around 35 times smaller than that of PL (Figure 5b). Figure 5c shows the output intensity of laser peak as a function of pumping density. Similar to the microscale devices, a superliner can be still seen at $6.9 \mu\text{J}/\text{cm}^2$, demonstrating the threshold behaviors well. The drastic changes in fwhm and power slope, associated with the bright spots in fluorescent microscope image (see inset in Figure 5c), confirm the lasing actions inside the tiny particle. In addition to the excitation with the ultrashort pulse laser, we also tried the pumping with a continuous-wave light source at 418 nm. Unfortunately, only the photoluminescence was achieved. This is mainly because the cavity lifetime is too short to generate enough gain with continuous-wave excitation. This might be solved by increasing the cavity lifetime via the combination of perovskite gain materials and high Q microcavities such as microsphere and microtoroids.

While the cavity size is close to lasing wavelength, this device does not operate with a single mode. This confirms again that the single mode laser emission in Figure 4b is not caused by the cavity size. To further understand the observed lasing modes, the optical resonances within the wavelength-scale particle were numerically studied. All of the results are summarized in Figure 5d. Within a wide spectral range from 510 to 560 nm, a series of resonant modes were obtained. Two of them have relatively high Q modes and wavelengths similar to those of the lasing modes. The Q factor of the mode at 544.6 nm is almost 330. The inset in Figure 5d is the corresponding field pattern where the electromagnetic field is mostly confined along the cavity boundary. Notably, the other high Q resonance has very similar field pattern. Their frequency difference is caused by the surface roughness. The longer wavelength mode is more confined within the raised scatters on the boundary and thus has lower Q factor. In any event, due to the rounded corners and convex boundaries, the resonances are closer to a WG mode instead of the diamond mode. Therefore, both of them are much higher than the Q factors of modes in perfect square cavity with the same size, and wavelength-scale perovskite laser with the smallest device size was experimentally demonstrated for the first time.

CONCLUSION

In summary, we prepared organo-lead halide perovskite films and studied the miscellaneous lasing actions within them. In

addition to the conventional understanding of random lasers, we show that each microparticle can generate laser emissions that are confined by total internal reflection along different orbits, e.g. the WG-like orbits and chaotic orbits. Considering the case that the sizes of different domains are randomly distributed, our results directly provide a different angle of view to understand the random distributed laser peaks in spectra that are obtained from a disorder perovskite film. Moreover, all three-dimensional wavelength-scale perovskite lasers have also been experimentally realized for the first time, which might be useful for the realization of highly integrated on-chip organo-lead halide perovskite lasers. While the fundamental bases of this research and previous reports are all whispering gallery modes, here, the lasing modes are mainly formed within the size-variable and irregular shaped microparticles. These observations can be important supplements to the conventional understanding of random lasers in perovskite films.

ASSOCIATED CONTENT

Supporting Information

The Supporting Information is available free of charge on the ACS Publications website at DOI: 10.1021/acsami.7b01383.

WG mode laser actions in other $\text{CH}_3\text{NH}_3\text{PbBr}_3$ particles and related simulations of resonant modes (PDF)

AUTHOR INFORMATION

Corresponding Authors

*E-mail: qinghai.song@hit.edu.cn.

*E-mail: shumixiao@hit.edu.cn.

ORCID

Shuai Wang: 0000-0001-6248-5267

Qinghai Song: 0000-0003-1048-411X

Shumin Xiao: 0000-0002-0751-9556

Notes

The authors declare no competing financial interest.

ACKNOWLEDGMENTS

The author would like to thank the financial support from National Natural Science Foundation of China under Grant 11374078, Shenzhen Fundamental research projects (JCYJ20160301154309393, JCYJ20160505175637639, and JCYJ20160427183259083), Public platform for fabrication and detection of micro- and nanosized aerospace devices, and Shenzhen engineering laboratory on organic-inorganic perovskite devices.

REFERENCES

- (1) Green, M. A.; Ho-Baillie, A.; Snaith, H. J. The Emergence of Perovskite Solar Cells. *Nat. Photonics* **2014**, *8*, 506–514.
- (2) Snaith, H. J. Perovskites: The Emergence of a New Era for Low-Cost, High-Efficiency Solar Cells. *J. Phys. Chem. Lett.* **2013**, *4*, 3623–3630.
- (3) Tan, Z. K.; Moghaddam, R. S.; Lai, M. L.; Docampo, P.; Higler, R.; Deschler, F.; Price, M.; Sadhanala, A.; Pazos, L. M.; Credgington, D.; Hanusch, F.; Bein, T.; Snaith, H. J.; Friend, R. H. Bright Light-Emitting Diodes Based on Organometal Halide Perovskite. *Nat. Nanotechnol.* **2014**, *9*, 687–692.
- (4) Stranks, S. D.; Snaith, H. J. Metal-Halide Perovskites for Photovoltaic and Light-Emitting Devices. *Nat. Nanotechnol.* **2015**, *10*, 391–402.
- (5) Yakunin, S.; Sytnyk, M.; Kriegner, D.; Shrestha, S.; Richter, M.; Matt, G. J.; Azimi, H.; Brabec, C. J.; Stangl, J.; Kovalenko, M. V.; Heiss,

W. Detection of X-ray Photons by Solution-Processed Lead Halide Perovskites. *Nat. Photonics* **2015**, *9*, 444–449.

(6) Song, J.; Xu, L.; Li, J.; Xue, J.; Dong, Y.; Li, X.; Zeng, H. Monolayer and Few-Layer All-Inorganic Perovskites as a New Family of Two-Dimensional Semiconductors for Printable Optoelectronic Devices. *Adv. Mater.* **2016**, *28*, 4861–4869.

(7) Xing, G.; Mathews, N.; Lim, S. S.; Yantara, N.; Liu, X.; Sabba, D.; Grätzel, M.; Mhaisalkar, S.; Sum, T. C. Low-Temperature Solution-Processed Wavelength-Tunable Perovskites for Lasing. *Nat. Mater.* **2014**, *13*, 476–480.

(8) Deschler, F.; Price, M.; Pathak, S.; Klintberg, L. E.; Jarausch, D. D.; Högler, R.; Hüttner, S.; Leijtens, T.; Stranks, S. D.; Snaith, H. J.; Atature, M.; Phillips, R. T.; Friend, R. H. High Photoluminescence Efficiency and Optically Pumped Lasing in Solution-Processed Mixed Halide Perovskite Semiconductors. *J. Phys. Chem. Lett.* **2014**, *5*, 1421–1426.

(9) Sutherland, B. R.; Hoogland, S.; Adachi, M. M.; Kanjanaboos, P.; Wong, C. T.; McDowell, J. J.; Xu, J.; Voznyy, O.; Ning, Z.; Houtepen, A. J.; Sargent, E. H. Perovskite Thin Films via Atomic Layer Deposition. *Adv. Mater.* **2015**, *27*, 53–58.

(10) Shi, D.; Adinolfi, V.; Comin, R.; Yuan, M.; Alarousu, E.; Buin, A.; Chen, Y.; Hoogland, S.; Rothenberger, A.; Katsiev, K.; Losovyj, Y.; Zhang, X.; Dowben, P. A.; Mohammed, O. F.; Sargent, E. H.; Bakr, O. M. Solar cells. Low Trap-State Density and Long Carrier Diffusion in Organolead Trihalide Perovskite Single Crystals. *Science* **2015**, *347*, 519–522.

(11) Zhang, N.; Wang, K.; Wei, H.; Gu, Z.; Sun, W.; Li, J.; Xiao, S.; Song, Q. Postsynthetic and Selective Control of Lead Halide Perovskite Microlasers. *J. Phys. Chem. Lett.* **2016**, *7*, 3886–3891.

(12) Pellet, N.; Teuscher, J.; Maier, J.; Grätzel, M. Transforming Hybrid Organic Inorganic Perovskites by Rapid Halide Exchange. *Chem. Mater.* **2015**, *27*, 2181–2188.

(13) Wong, A. B.; Lai, M.; Eaton, S. W.; Yu, Y.; Lin, E.; Dou, L.; Fu, A.; Yang, P. Growth and Anion Exchange Conversion of $\text{CH}_3\text{NH}_3\text{PbX}_3$ Nanorod Arrays for Light-Emitting Diodes. *Nano Lett.* **2015**, *15*, 5519–5524.

(14) Solis-Ibarra, D.; Smith, I. C.; Karunadasa, H. I. Post-synthetic Halide Conversion and Selective Halogen Capture in Hybrid Perovskites. *Chem. Sci.* **2015**, *6*, 4054–4059.

(15) Zhang, Q.; Ha, S. T.; Liu, X.; Sum, T. C.; Xiong, Q. Room-Temperature Near-Infrared High-Q Perovskite Whispering-Gallery Planar Nanolasers. *Nano Lett.* **2014**, *14*, 5995–6001.

(16) Liao, Q.; Hu, K.; Zhang, H.; Wang, X.; Yao, J.; Fu, H. Perovskite Microdisk Microlasers Self-Assembled from Solution. *Adv. Mater.* **2015**, *27*, 3405–3410.

(17) Ha, S. T.; Liu, X.; Zhang, Q.; Giovanni, D.; Sum, T. C.; Xiong, Q. Synthesis of Organic-Inorganic Lead Halide Perovskite Nanoplatelets: Towards High-Performance Perovskite Solar Cells and Optoelectronic Devices. *Adv. Opt. Mater.* **2014**, *2*, 838–844.

(18) Zhu, H.; Fu, Y.; Meng, F.; Wu, X.; Gong, Z.; Ding, Q.; Gustafsson, M. V.; Trinh, M. T.; Jin, S.; Zhu, X. Y. Lead Halide Perovskite Nanowire Lasers with Low Lasing Thresholds and High Quality Factors. *Nat. Mater.* **2015**, *14*, 636–642.

(19) Gu, Z. Y.; Wang, K. Y.; Sun, W. Z.; Li, J. K.; Liu, S.; Song, Q. H.; Xiao, S. M. Two-Photon Pumped $\text{CH}_3\text{NH}_3\text{PbBr}_3$ Perovskite Microwire Lasers. *Adv. Opt. Mater.* **2016**, *4*, 472–479.

(20) Wang, K.; Gu, Z.; Liu, S.; Li, J.; Xiao, S.; Song, Q. Formation of Single-Mode Laser in Transverse Plane of Perovskite Microwire via Micromanipulation. *Opt. Lett.* **2016**, *41*, 555–558.

(21) Wang, K.; Gu, Z.; Liu, S.; Sun, W.; Zhang, N.; Xiao, S.; Song, Q. High-Density and Uniform Lead Halide Perovskite Nanolaser Array on Silicon. *J. Phys. Chem. Lett.* **2016**, *7*, 2549–2555.

(22) Wang, K.; Sun, W.; Li, J.; Gu, Z.; Xiao, S.; Song, Q. Unidirectional Lasing Emissions from $\text{CH}_3\text{NH}_3\text{PbBr}_3$ Perovskite Microdisks. *ACS Photonics* **2016**, *3*, 1125–1130.

(23) Gu, Z.; Sun, W.; Wang, K.; Zhang, N.; Zhang, C.; Lyu, Q.; Li, J.; Xiao, S.; Song, Q. Hybridizing $\text{CH}_3\text{NH}_3\text{PbBr}_3$ Microwires and Tapered Fibers for Efficient Light Collection. *J. Mater. Chem. A* **2016**, *4*, 8015–8019.

(24) Whitworth, G. L.; Harwell, J. R.; Miller, D. N.; Hedley, G. J.; Zhang, W.; Snaith, H. J.; Turnbull, G. A.; Samuel, I. D. W. Nanoimprinted Distributed Feedback Lasers of Solution Processed Hybrid Perovskites. *Opt. Express* **2016**, *24*, 23677–23684.

(25) Saliba, M.; Wood, S. M.; Patel, J. B.; Nayak, P. K.; Huang, J.; Alexander-Webber, J. A.; Wenger, B.; Stranks, S. D.; Horantner, M. T.; Wang, J. T.; Nicholas, R. J.; Herz, L. M.; Johnston, M. B.; Morris, S. M.; Snaith, H. J.; Riede, M. K. Structured Organic-Inorganic Perovskite toward a Distributed Feedback Laser. *Adv. Mater.* **2016**, *28*, 923–929.

(26) Jia, Y.; Kerner, R. A.; Grede, A. J.; Brigeman, A. N.; Rand, B. P.; Giebink, N. C. Diode-Pumped Organo-Lead Halide Perovskite Lasing in a Metal-Clad Distributed Feedback Resonator. *Nano Lett.* **2016**, *16*, 4624–4629.

(27) Chen, S.; Roh, K.; Lee, J.; Chong, W. K.; Lu, Y.; Mathews, N.; Sum, T. C.; Nurmikko, A. A Photonic Crystal Laser from Solution Based Organo-Lead Iodide Perovskite Thin Films. *ACS Nano* **2016**, *10*, 3959–3967.

(28) Dhanker, R.; Brigeman, A. N.; Larsen, A. V.; Stewart, R. J.; Asbury, J. B.; Giebink, N. C. Random Lasing in Organo-Lead Halide Perovskite Microcrystal Networks. *Appl. Phys. Lett.* **2014**, *105*, 151112.

(29) Liu, S.; Sun, W.; Li, J.; Gu, Z.; Wang, K.; Xiao, S.; Song, Q. Random Lasing Actions in Self-Assembled Perovskite Nanoparticles. *Opt. Eng.* **2016**, *55*, 057102.

(30) Yakunin, S.; Protesescu, L.; Krieg, F.; Bodnarchuk, M. I.; Nedelcu, G.; Humer, M.; De Luca, G.; Fiebig, M.; Heiss, W.; Kovalenko, M. V. Low-Threshold Amplified Spontaneous Emission and Lasing from Colloidal Nanocrystals of Caesium Lead Halide Perovskites. *Nat. Commun.* **2015**, *6*, 8056.

(31) Song, Q.; Liu, L.; Xiao, S.; Zhou, X.; Wang, W.; Xu, L. Unidirectional High Intensity Narrow-Linewidth Lasing from a Planar Random Microcavity Laser. *Phys. Rev. Lett.* **2006**, *96*, 033902.

(32) Wiersma, D. S. Disordered Photonics. *Nat. Photonics* **2013**, *7*, 188–196.

(33) Cao, H.; Zhao, Y. G.; Ho, S. T.; Seelig, E. W.; Wang, Q. H.; Chang, R. P. H. Random Laser Action in Semiconductor Powder. *Phys. Rev. Lett.* **1999**, *82*, 2278–2281.

(34) Shao, Y.; Fang, Y.; Li, T.; Wang, Q.; Dong, Q.; Deng, Y.; Yuan, Y.; Wei, H.; Wang, M.; Gruverman, A.; Shield, J.; Huang, J. Grain Boundary Dominated Ion Migration in Polycrystalline Organic-Inorganic Halide Perovskite Films. *Energy Environ. Sci.* **2016**, *9*, 1752–1759.

(35) Yuan, Y.; Huang, J. Ion Migration in Organometal Trihalide Perovskite and Its Impact on Photovoltaic Efficiency and Stability. *Acc. Chem. Res.* **2016**, *49*, 286–293.

(36) Xia, B.; Wu, Z.; Dong, H.; Xi, J.; Wu, W.; Lei, T.; Xi, K.; Yuan, F.; Jiao, B.; Xiao, L.; Gong, Q.; Hou, X. Formation of Ultrasmooth Perovskite Films toward Highly Efficient Inverted Planar Heterojunction Solar Cells by Micro-Flowing Anti-Solvent Deposition in Air. *J. Mater. Chem. A* **2016**, *4*, 6295–6303.

(37) Cao, H.; Wiersig, J. Dielectric Microcavities: Model Systems for Wave Chaos and Non-Hermitian Physics. *Rev. Mod. Phys.* **2015**, *87*, 61–111.

(38) Huang, Y. Z.; Che, K. J.; Yang, Y. D.; Wang, S. J.; Du, Y.; Fan, Z. C. Directional Emission InP/GaInAsP Square-Resonator Microlasers. *Opt. Lett.* **2008**, *33*, 2170–2172.

(39) Kumawat, N. K.; Dey, A.; Narasimhan, K. L.; Kabra, D. Near Infrared to Visible Electroluminescent Diodes Based on Organometallic Halide Perovskite: Structural and Optical Investigation. *ACS Photonics* **2015**, *2*, 349–354.

(40) Podolskiy, V. A.; Narimanov, E.; Fang, W.; Cao, H. Chaotic Microlasers Based on Dynamical Localization. *Proc. Natl. Acad. Sci. U. S. A.* **2004**, *101*, 10498–10500.

(41) Song, Q. H.; Ge, L.; Stone, A. D.; Cao, H.; Wiersig, J.; Shim, J. B.; Unterhinninghofen, J.; Fang, W.; Solomon, G. S. Directional Laser Emission from a Wavelength-Scale Chaotic Microcavity. *Phys. Rev. Lett.* **2010**, *105*, 103902.

(42) Ma, X. W.; Huang, Y. Z.; Yang, Y. D.; Xiao, J. L.; Weng, H. Z.; Xiao, Z. X. Mode Coupling in Hybrid Square-Rectangular Lasers for Single Mode Operation. *Appl. Phys. Lett.* **2016**, *109*, 071102.

(43) Wang, K.; Sun, W.; Wang, S.; Liu, S.; Zhang, N.; Xiao, S.; Song, Q. Single Crystal Microrod Based Homonuclear Photonic Molecule Lasers. *Adv. Opt. Mater.* **2017**, *5*, 1600744.

www.spm.com.cn